JOURNAL OF AIRCRAFT
Vol. 47, No. 5, September–October 2010

Helicopter Rotor Shape Optimization for the Improvement of Aeroacoustic Performance in Hover

Sanghyun Chae* and Kwanjung Yee†
Pusan National University, Busan 609-735, Republic of Korea
Choongmo Yang‡ and Takashi Aoyama§
Japan Aerospace Exploration Agency (JAXA), Tokyo 182-8522, Japan
and
Shinkyu Jeong¶ and Shigeru Obayashi**
Tohoku University, Miyagi 908-8577, Japan

DOI: 10.2514/1.C000283

A helicopter rotor is optimally designed for aeroacoustic performance improvement. As shown in previous reports, the blade shapes can be designed to minimize high-speed impulsive noise but tend to have excessively high tapers and be swept back. Since an overly short chord length around the blade-tip region may cause structural problems and safety issues in autorotation, an autorotation index has been introduced to keep the tip region from having excessive taper ratios. In addition, the changes in thickness and camber of the airfoils can also be taken into account to better represent realistic rotor shapes. Aeroacoustic analysis is performed using Kirchhoff's method coupled with computational fluid dynamics analysis, and the optimization is performed using the kriging-model-based genetic algorithm method. Optimization results are presented that show that the designed blades have improved aerodynamic performance and reduced high-speed impulsive noise characteristics. It is found that a more practical blade shape can be obtained by using airfoil transitions and an autorotation index. The results of the analysis of variance and self-organization map indicate that the taper ratios, the swept back, the tip chord length, the protrusion shape, the camber, and the thickness of the root airfoil are the prominent features affecting the aeroacoustic performance of the rotor.

Nomenclature

A	=	rotor disk area, m^2
C_{P_i}	=	induced power coefficient
c	=	chord length of the baseline, m
$f_{\min}$	=	minimum value among n sampled values
I_R	=	moment of rotational inertia, kg $\cdot$ m^2
R	=	rotor radius, m
$S(x)$	=	root-mean-squared error of kriging model
W	=	weight of helicopter, N
$\mathbf{x}$	=	m-dimensional vector
$y(x)$	=	unknown function, the real function
$\hat{y}(x)$	=	kriging prediction
$Z(\mathbf{x})$	=	local deviation from the global model
β	=	global model constant
σ	=	standard deviation
Φ	=	cumulative distribution function
ϕ	=	probability density function
Ω	=	angular velocity, rad/s

Received 29 January 2010; revision received 27 May 2010; accepted for publication 28 May 2010.

*Graduate Student, Department of Aerospace Engineering, San 30 Jangjeon 2(i)-dong Geumjong-gu.

†Associate Professor, Department of Aerospace Engineering; daedalus@pusan.ac.kr. Member AIAA.

‡Research Engineer, Numerical Analysis Group; currently Research Institute of Industrial Science and Technology, Pohang, Republic of Korea. Member AIAA.

§Research Engineer, Numerical Analysis Group, Chofu. Member AIAA.

¶Associate Professor, Institute of Fluid Science, Sendai-shi. Member AIAA.

**Professor, Institute of Fluid Science. Member AIAA.

I. Introduction

NOISE issues have been a serious impediment to the public acceptance of helicopters, as well as their effect on passenger comfort. As shown in Fig. 1 [1], the helicopter has various noise sources resulting from the aerodynamic interactions between the rotor wakes and other solid surfaces. Among these noise sources, high-speed impulsive (HSI) noise is considered to be the most significant due to its impulsive and annoying nature, caused by shock waves on the blade surface on the advancing side, as shown in Fig. 2. It is evident from the figure that the relative inflow Mach number of the rotating blade increases along the blade span, from the root to the tip. Even though the Mach line, where the relative Mach number reaches unity, is located beyond the blade tip, strong disturbances caused by the shock wave near the blade tip propagate to far-field regions as noise. Such loud noise could cause detectability concerns during high-speed forward flight, and so it limits the urban accessibility of helicopters.

Earlier studies [2,3] of helicopter noise have proposed the blade thickness noise as the source for high-speed blade slap, now referred to as HSI noise, and by the 1980s, advances in theoretical approaches, combined with several model-scale experiments and flight tests, have led to a fair understanding of the physics behind HSI noise. Schmitz and Yu [4] reviewed the status of these studies during that decade. For the prediction of rotor noise, the Ffowcs Williams and Hawkings (FW–H) equation [5] has often been solved, since this is able to predict the noise from a subsonic rotor quite well [6–8]. In the late 1980s, the Kirchhoff formulation was introduced as a new approach together with computational fluid dynamics (CFD) analysis, which made use of the significant advances in computing power, the approach uses a Kirchhoff surface, on which all the acoustic sources are enclosed. The Kirchhoff method can capture the acoustic pressure related to the HSI noise, if the CFD solution on the properly chosen Kirchhoff surface includes a shock wave. Although the FW–H equation has a better flexibility in the choice of the control surface (Kirchhoff surface) than the Kirchhoff method, it is difficult to evaluate the quadrupole term of the FW–H equation on the HSI noise prediction [9–12]. George and Lyrintzis [13,14] suggested the

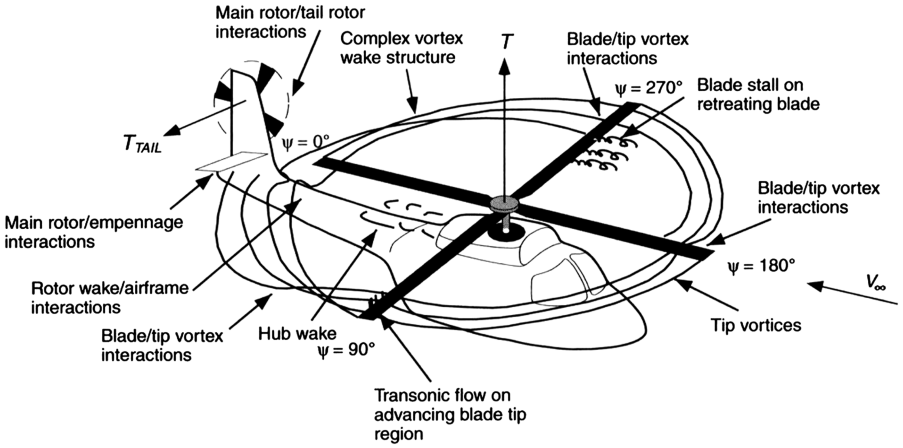

Fig. 1 Various noise sources in helicopters [1].

Kirchhoff method, which extends the computed two-dimensional midfield results to the three-dimensional far field for the blade–vortex interactions (BVI) noise prediction. Xue and Lyrintzis [15] predicted three-dimensional BVI noise using the unsteady transonic full-potential rotor code and the rotating Kirchhoff method. Lyrintzis [16] also provided a comprehensive review on the use of the Kirchhoff method in computational aeroacoustics. By using these noise-prediction methods, the studies about the HSI noise prediction [4,17,18] have shown that modifications to the blade planform near the tip can reduce the HSI noise intensity. Parametric studies or optimization techniques have been carried out in order to produce better blade planform designs and so reduce the HSI noise. Baeder et al. [19] investigated the effect of blade-tip shapes of a helicopter rotor on the near-field and the far-field HSI noise. Using a CFD code for the near-field solution and a Kirchhoff solver for the far-field acoustic solution, a series of parametric studies was conducted to find the noise-generating mechanisms of various blade planforms to reduce the HSI noise. Aoyama et al. [20] validated the CFD code with measured data [21] to predict the HSI noise, and they used this to search for a better blade planform through parametric studies. It has been concluded that a shock wave on the blade surface, the location of the shock, and the area of the supersonic region in the vicinity of the blade tip are the dominant factors affecting HSI noise intensity.

However, parametric studies have an inherent limitation in determining the optimal blade planform for reducing HSI noise, which is the difficulty in choosing appropriate design parameters. With increasing computing power and advances in computational techniques, blade design optimization using CFD has become an inevitable tool in aerodynamics, even though high-fidelity CFD solvers are still severely limited by their computational cost. To date, most research studies on blade planform optimization have been targeted toward performance enhancement, and little attention has been paid to the HSI noise problem. Jones et al. [22] attempted the rotorcraft airfoil designs with the HSI noise reduction included, using the codes XFOIL, WOPWOP, and the parallel genetic algorithm (GA). Nontraditional airfoil shapes were obtained, which offered good aerodynamic and aeroacoustic performance. However, the study did not go further to include the performance analysis of the three-dimensional rotors with the result airfoils. Lee and Kwon [23] used optimization techniques to obtain an optimal rotor blade configuration, which minimized the required inviscid torque under the constraint of maintaining the desired thrust level. Le Pape [24] presented a multiobjective procedure to optimize rotor blade shapes for hover and forward flight performances, simultaneously. Again, the study focused on performance improvement alone. Xue et al. [25] developed an integrated aeroacoustics rotor simulation methodology, which coupled a comprehensive rotorcraft analysis code (COPTER) and a full-potential code for unsteady three-dimensional transonic flows around rotor blades, but the shock wave from the potential code was not strong enough for significant HSI noise effects. Collins et al. [26] attempted to redesign the higher-harmonic control aeroacoustic rotor test model rotor, based on the Pareto frontier method, by using both low- and high-fidelity analysis tools. However, this research showed the redesign of a rotor similar to the BO-105 alone, using simple shape design variables (DVs).

In this study, a series of optimization designs have been conducted with the main objective being to reduce the HSI noise of a rotor blade. To this end, a high-fidelity aeroacoustic analysis tool and efficient optimization techniques are employed, and the DVs are carefully designated to describe an arbitrary planform shape. The first attempt [27] is to design a blade shape for HSI noise reduction by varying the blade planform only. The resulting blade shapes have shown considerable reduction of HSI noise with high taper ratio and being swept back at the tip region, as shown in Fig. 3a. However, an excessively short chord length near the tip may cause structural problems and flight safety issues in autorotation. Hence, in later research [28], a second objective to increase blade loading is imposed for a given thrust level, as this objective may prevent a designed shape from having excessively short chord lengths near the blade tip, because the blade sections near the tip generate higher loads than at other parts. More DVs are added to allow the change of airfoils along the span, with different thicknesses. Although the designed shapes

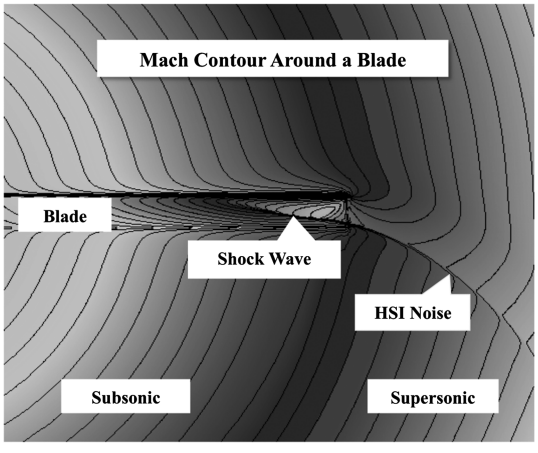

Fig. 2 HSI noise generation.

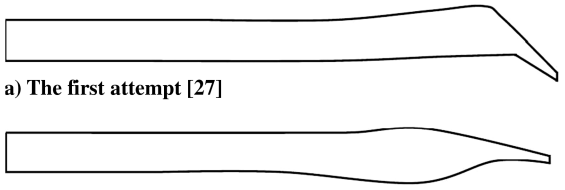

a) The first attempt [27]

b) Later work [28]

Fig. 3 Previously designed shapes.

are obtained for improving the aeroacoustic performance, the same problems are observed, as shown in Fig. 3b.

To cope with this problem, an autorotation index (AI) is considered as a new design constraint to make the blade retain sufficient moment of inertia at the tip region; this is expected to prevent the blade volume at the tip region from becoming excessively low. To design a more practical blade, the second objective is modified, as the induced power of the rotor blade and additional DVs, which include the change in the airfoil section, are used with the existing DVs for producing arbitrary planforms. As will be shown later, these modifications to the design problem are crucial in producing more practical and advanced design shapes with enhanced performances.

To evaluate the aerodynamic performance, Euler-equation-based CFD are used, and Kirchhoff's method predicts the aeroacoustic pressure on the far field for the evaluation of the HSI noise; the numerical methods for the CFD and the HSI noise calculations are introduced in the next section. A GA coupled with a surrogate model is chosen as an efficient optimization technique to solve the arising multiobjective design problem. This optimization method is briefly described in the following section, and the definitions of the design problem, including the modification and supplements of the present work, are explained in Sec. IV, followed by an explanation of the design results, the effects of the design problem modification, and the relations among the DVs and the objectives in Sec. V.

II. Aerodynamics and Acoustics

A. Numerical Methods

For the prediction of the near-field sound pressure and the evaluation of the hovering performance, a series of numerical analyses are carried out to determine the exact flowfield around the rotor blade. The governing equations of the CFD solver are the three-dimensional unsteady Euler equations in the blade-fixed rotating Cartesian coordinate system (x, y, z). To conduct the calculations with an arbitrary curved grid, these equations are transformed from the Cartesian coordinate system to an arbitrary curvilinear coordinate system (ξ, η, ζ). A schematic representation of the Cartesian and the curvilinear coordinate systems of the rotating blade are shown in Fig. 4. An implicit finite-difference scheme is used to solve the governing equations, and the Beam–Warming scheme, coupled with the total variation diminishing scheme, is employed for the spatial discretization, where the MUSCL approach is used with a minmod limiter. For temporal integration, the Euler backward implicit and the Newton subiteration methods in unsteady calculation are used where the numerical schemes use second-order approximations in space and first-order approximations in time. The upwind line Gauss–Seidel relaxation method is used as the solution algorithm, and the specific details of the CFD solver have been reported in a previous paper [29].

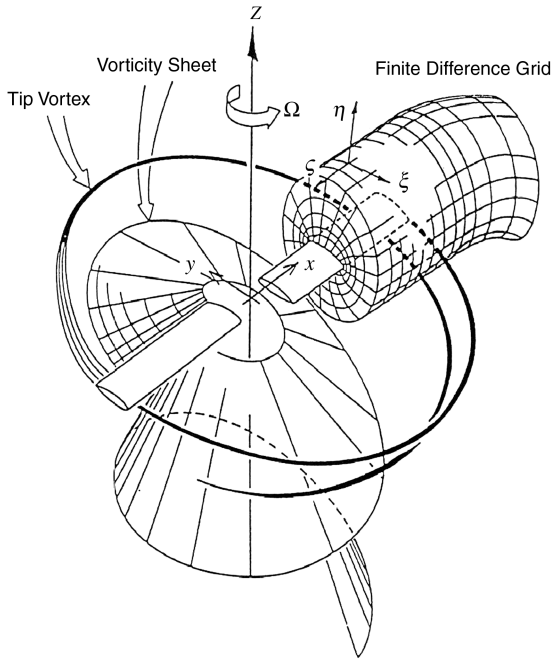

Fig. 4 Blade coordinates system and grid [11,21].

Figures 5a and 5b show the overall perspective and the top views of the O-H type of grid system that have been used for the computations where the baseline blade has a rectangular planform similar to that of UH-1 and is further modified during the shape optimization process. Figure 5c shows one example of an arbitrary planform.

The grid consists of 922,500 points ($123 \times 50 \times 150$: chordwise $\times$ normal $\times$ spanwise), and 12,300 points (123×100: chordwise $\times$ spanwise) are distributed along the blade surface. The outboard of the blade tip is swept back to follow the shock wave, which propagates to the far field as HSI noise.

B. Acoustics

The near-field acoustic characteristics are predicted based on the pressure results from the CFD computations. For the far-field acoustic predictions, the CFD method coupled with Kirchhoff's equation [6,30,31] is used. In this method, after the pressure distribution around a rotor blade is obtained using CFD analysis, the Kirchhoff equation, extended for a moving surface, is solved to determine the acoustic pressure at a far-field observer position. The solutions of the Euler equations on the Kirchhoff surface, on which all the acoustic sources are enclosed, are used as the source pressure data, as shown in Fig. 6. If the CFD analysis takes into account all the nonlinear effects within the Kirchhoff surface, this method can capture the acoustic pressure at any given far-field location. The Kirchhoff surface in the x axis is positioned at about a 1.1 rotor radius, and the apsidal line is about four blade chords away from the surface. The details of this method have been described in [20].

III. Optimization Method

For the modification of the blade shape to improve the acoustic and aerodynamic performances, an optimization method should be combined with the CFD flow solver in some manner. In the present study, the CFD solver is weakly coupled with the optimization method through surrogate models (namely, the kriging model), and the optimization method is selected for its computational efficiency.

Since the required computation resource and the numerical complication rapidly grow with the number of DVs, it is necessary to find an efficient optimization method when handling a realistic engineering problem. To achieve this, a surrogate model based on the GA is selected, where the GA conducts the optimization based on the surrogate models rather than on the CFD analysis module; that is, the actual CFD calculations are replaced by appropriate surrogate models, which can greatly reduce the computational time on the optimization process.

In this study, the GA method using the kriging model, which has been presented in the literature (see, for example, [32–34]), has been chosen, as it is one of the most widely used surrogate models, and it is designed to predict the distribution function at an unknown point instead of the function value itself. Such a surrogate model approach has attracted a lot of attention in the field of aircraft design, due to its significant reduction in the computational time needed to evaluate the objective function. However, there is a common drawback to this approach; namely, the possibility that the true optimum in the design space might be missed if the optimization relies on the estimated function values of the approximation model alone, because such values include a degree of uncertainty. To overcome this shortfall, an additional criterion of expected improvement (EI) is used in the GA exploration, so that the EI predicts the function value and its uncertainty at unknown points based on the distribution of the function values. By selecting the maximum EI point as an additional sample point in the kriging model, the accuracy and a level of robustness in the search for the true optimum can be sequentially improved simultaneously.

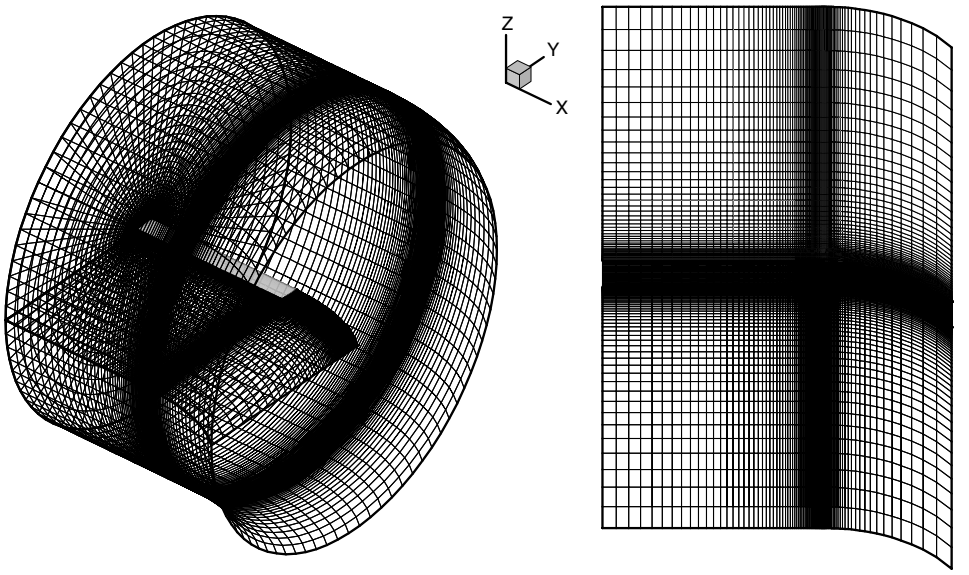

a) Three-dimensional view of the blade grid

b) Top view of the rectangular blade grid

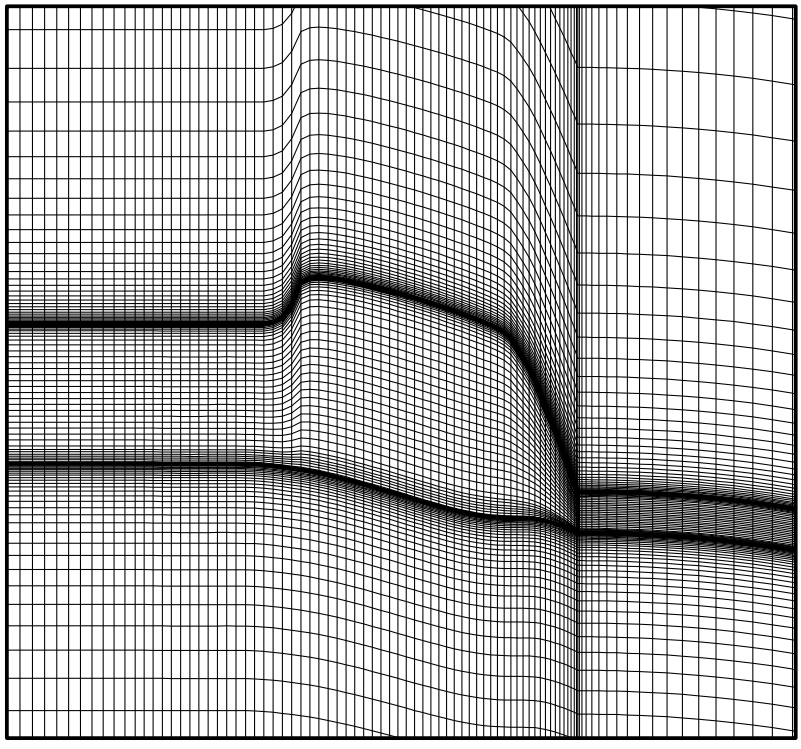

c) Top view of an arbitrary blade grid around the tip

Fig. 5 Grid system.

A. Kriging Model

First, the kriging model is constructed, based on the computation results at sample points, as the predictor of the objective function. The model assumes the unknown function, $y(\mathbf{x})$, as

$$y(\mathbf{x}) = \beta + Z(\mathbf{x}) \tag{1}$$

where $\mathbf{x}$ is an m-dimensional vector (m DVs), β is a global model constant, and $Z(\mathbf{x})$ represents the local deviation from the global model. In the model, the local deviation at an unknown point $\mathbf{x}$ is expressed using stochastic processes. The sample points are interpolated using a Gaussian random function as the correlation function to estimate the trend of the stochastic processes, and the correlation between $Z(\mathbf{x}^i)$ and $Z(\mathbf{x}^j)$ is strongly related to the distance between the two corresponding points, $\mathbf{x}^i$ and $\mathbf{x}^j$. By using the specially weighted distance and the Gaussian random function, the correlation between points $\mathbf{x}^i$ and $\mathbf{x}^j$ is defined.

The accuracy of the predicted value largely depends on the distance from the sample points. Intuitively, the closer the point $\mathbf{x}$ is located to the sample point, the more accurate is the prediction from the kriging model $\hat{y}(\mathbf{x})$.

B. Expected Improvement

Once the approximation model is constructed, the optimum value is searched by applying an arbitrary optimizer. To find the global optimum in the kriging model, both the estimated function value and its uncertainty at the unknown point are considered at the same time. Based on these values, the point having the highest probability of being the global optimum is quantified in terms of the EI [35].

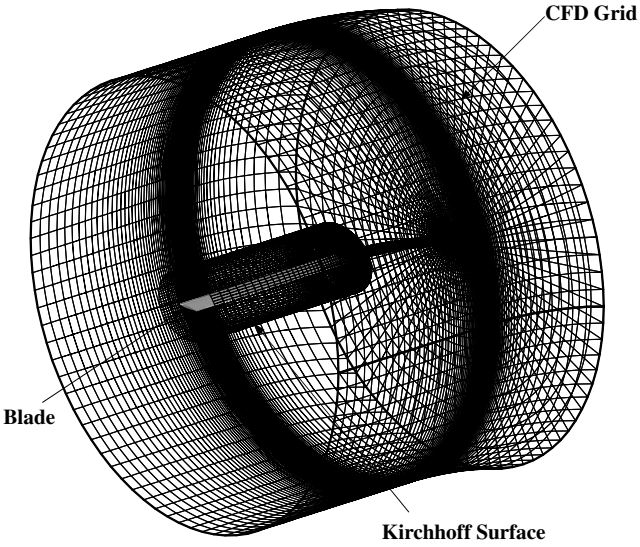

Fig. 6 Kirchhoff surface in the grid system.

The EI of the minimization problem can be calculated as follows:

$$E[I] = (f_{\min} - \hat{y})\Phi\left(\frac{f_{\min} - \hat{y}}{s}\right) + s\phi\left(\frac{f_{\min} - \hat{y}}{s}\right) \tag{2}$$

where $f_{\min}$ is the minimum value among n sampled values, and the values Φ and ϕ are the standard distribution, and the normal density s is the root-mean-squared error, respectively.

C. Genetic Algorithm

As already stated, to select the maximum EI value point in the design space, a GA [36] is employed. GAs are a particular class of evolutionary algorithms inspired by evolutionary biology, with key features such as inheritance, mutation, selection, and crossover included in a mathematical setting of the optimization problem. The evolution usually starts from a population of randomly generated individuals and continues through iterations of the algorithm, which are referred to as generations.

In each generation, the fitness of every individual in the population is evaluated, and multiple individuals are stochastically selected from the current population. These are recombined and randomly mutated to form a new population, which is then used again in the next iteration of the algorithm. It should be noted that the value of the objective function itself (not its derivative) is used in the GA approach, which means the objective does not need to be differentiated. Another merit of a GA is that it searches for the optimum point from multiple points of the population, not a single point. This feature makes GAs robust and attractive to aerodynamic design problems, where nonlinearities, multimodalities, and discontinuities are most likely to exist.

D. Overall Procedure of the Kriging-Model-Based Genetic Algorithm Method

The overall procedure of the optimization, shown in Fig. 7, is as follows:

1) Initial sample points are selected by an improved distributed sampling [37].
2) The CFD solver evaluates the sample points.
3) The kriging model is constructed with the sample points.
4) The GA starts. Initially 512 populations are generated and evaluated using the kriging model.
5) The parents are selected.
6) Crossover and mutations transpire.
7) The fitness of the new generation is evaluated.
8) If the number of generations does not exceed 100, repeat the procedure from step 4.
9) Additional sample points may be selected using the EI by the user.
10) Repeat the procedure from step 2 until the optima of the kriging model are not updated over five iterations.

IV. Definition of the Design Problem

It has been reported in a previous study that the rotor blade design shapes still contain excessively short chord lengths near the tip region, which may cause structural problems and flight safety issues in the autorotation. To overcome the poor moment of inertia at the tip region, as well as to obtain more realistic blade shapes, some modifications have been made to this previous work, such as changing the objective function and including more DVs and additional constraints.

A. Design Objective Functions

For noise reduction, the absolute value of the minimum acoustic pressure is set as the main objective function, as in previous research [27,28]. The objective function aims to improve the HSI noise characteristics by reducing the absolute peak of the acoustic pressure at the evaluation point, $r = 1.11R$, near the blade tip. The modified objective function for considering the aerodynamic characteristics is the induced power coefficient of a designed blade. Since the Euler solver is incapable of taking viscous effects into account, the power obtained from the computations is entirely induced power for which the coefficient is written as

$$C_{P_i} = \frac{\text{induced power}}{\rho A \Omega^2 R^3} \tag{3}$$

where $A = \pi R^2$, Ω, and R are the mean rotor disk area, the angular velocity, and the rotor radius, respectively.

Table 1 shows some specific calculation conditions and the fixed shape parameters. The induced power is calculated when the tip Mach number is 0.667 and the target thrust coefficient is defined as 0.0046. These tip speed and thrust values are those of a hovering helicopter, UH-1H.

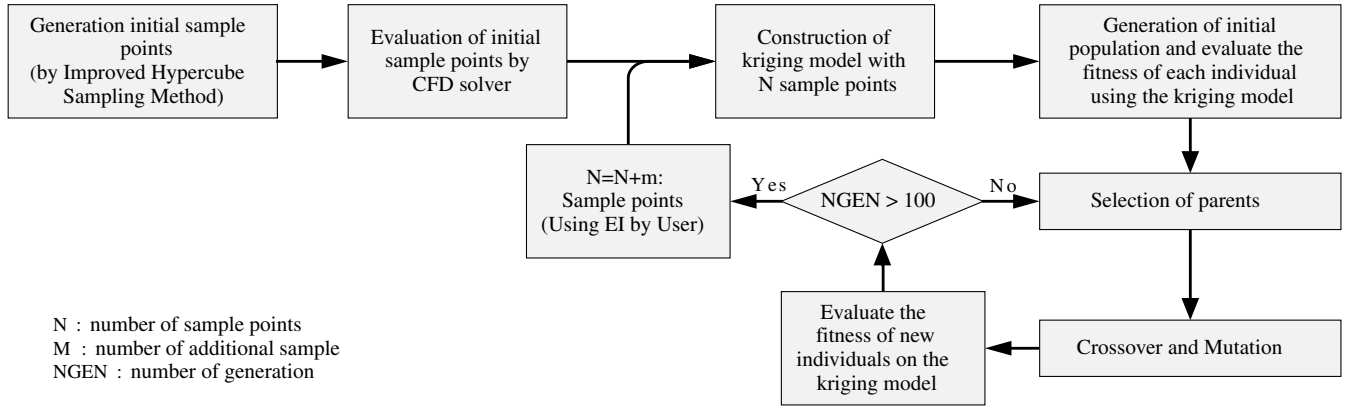

Fig. 7 Optimization procedure of the kriging-model-based GA method.

Table 1 Calculation conditions and the shape parameters

Parameter	HSI noise	Induced power
Tip Mach number	0.9	0.667
Aspect ratio	13.7	13.7
Linear twist	−10.9°	−10.9°

B. Design Variables

Figure 8 shows the definition of the DVs where 10 control points (five points each for the leading and trailing edges) with 14 DVs define the desired blade planform. The blade length is kept constant by fixing the spanwise positions of points 5 and 6. The relative order of the neighboring points defining the blade geometry is summarized in Table 2, where the 18 DVs are divided into three groups that are the leading edge, the tip, and the trailing edge. The five control points in the leading-edge group range from DV 1 to DV 7, and those in the trailing edge group are from DV8 to DV14. Any two neighboring points are connected by a cubic B-spline curve, starting from points 2 and 9. Points 1 and 10 are used to compute the initial gradient while generating the spline curves between points 2 and 3 and points 11 and 10, respectively. The minimum distance between any two neighboring points is limited for practical reasons to avoid excessive twists in the curves. The tip edge is constrained to have a straight line, which is defined by two points: DV9 and DV10. For practical consideration concerning grid generation and blade manufacturing, the minimum chord length of the tip edge is limited to $0.15c$, where c is the blade chord length.

Unlike in previous studies, novel DVs are added to change the airfoil shape (NACA four-digit airfoils) at the root and the tip, where these airfoils are defined by using simple polynomial equations that generate an airfoil section using maximum camber, maximum camber location, and maximum thickness as input variables. To simplify the problem, only the thickness and camber of an airfoil at the root and the tip (that is, a total of four DVs) are considered in the present work, so that the airfoil shapes at the root and the tip are changed during the design iteration. The boundaries of additional DVs (DV15 ∼ DV18) are presented in Table 2. The transition range between the two airfoils is $0.1R$, and its center is defined as the 19th DV. The combination of the airfoil sections is introduced to consider the different aerodynamic characteristics along the blade span due to blade rotation, and the boundary of this last DV is presented in Table 2.

C. Design Constraints

In addition to the geometric relations between neighboring points, two more constraints are applied: the first is to impose a limit in the change of the blade planform area, and the second is a limit to the curvature of the planform shape, from a practical viewpoint. The area constraint restricts the allowable variation of the planform area of the designed blade and, considering the area change of a British Experimental Rotor Programme (BERP)-type blade with respect to the rectangular blade, as shown in Fig. 9, around a 4% variation of the planform area is tolerated during the optimization process. The BERP-type blade planform is regarded as a reference because it has quite a large area change near the tip.

Table 2 Design constraints for the relative geometric positions of the DVs

Variables	Description	Constraint
DV1	X position of point 1	$0.0R \le \text{DV1} \le 0.5R$
DV2	X position of point 2	$0.5R \le \text{DV2} \le \text{DV3}$
DV3	X position of point 3	$\text{DV2} \le \text{DV3} \le \text{DV5}$
DV4	Y position of point 3	$-0.3c \le \text{DV4} \le 0.4c$
DV5	X position of point 4	$\text{DV3} \le \text{DV5} \le 0.98R$
DV6	Y position of point 4	$-0.3c \le \text{DV6} \le 0.4c$
DV7	Y position of point 5	$\text{DV7} \le \text{DV8} \le 0.5c$
DV8	Y position of point 6	$-1.5c \le \text{DV7} \le \text{DV8}$
DV9	X position of point 7	$\text{DV11} \le \text{DV9} \le 0.98R$
DV10	Y position of point 7	$-1.4c \le \text{DV10} \le -0.7c$
DV11	X position of point 8	$\text{DV13} \le \text{DV11} \le \text{DV9}$
DV12	Y position of point 8	$-1.4c \le \text{DV12} \le -0.7c$
DV13	X position of point 9	$0.5R \le \text{DV13} \le \text{DV11}$
DV14	X position of point 10	$0.0R \le \text{DV14} \le 0.5R$
DV15	Camber of root airfoil	$0.0c \le \text{DV15} \le 0.04c$
DV16	Thickness of root airfoil	$0.08c \le \text{DV16} \le 0.15c$
DV17	Camber of tip airfoil	$0.0c \le \text{DV17} \le 0.04c$
DV18	Thickness of tip airfoil	$0.08c \le \text{DV18} \le 0.15c$
DV19	Airfoil Transition	$0.5R \le \text{DV19} \le 0.95R$

Randomly generated blade planforms may have strange or unacceptable shapes, with extremely small chord lengths or excessive curvatures, as demonstrated in Fig. 10. More geometric constraints are applied to avoid these impractical blade shapes during the optimization process.

The AI [1] is introduced as a new constraint in the present research, and it provides a relative measure to show the autorotation characteristics of the blades; it is expressed as follows:

$$\text{AI} = \frac{I_R \Omega^2}{2W \cdot DL} \tag{4}$$

where I_R, Ω, W, and DL are the mean moment of the rotational inertia, the rotational speed, the weight of the vehicle, and the disk loading, respectively.

In autorotation, it is crucial to maintain the rotational speed for the first few seconds, and this is more easily achieved when the blade has

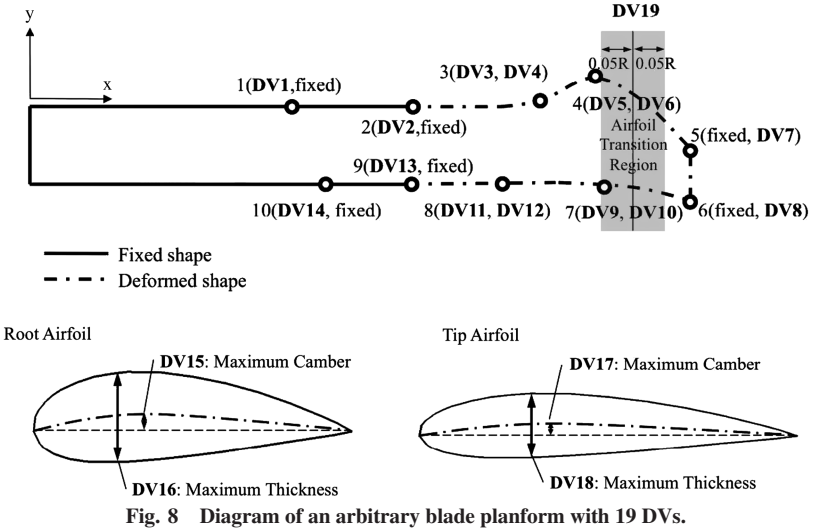

Fig. 8 Diagram of an arbitrary blade planform with 19 DVs.

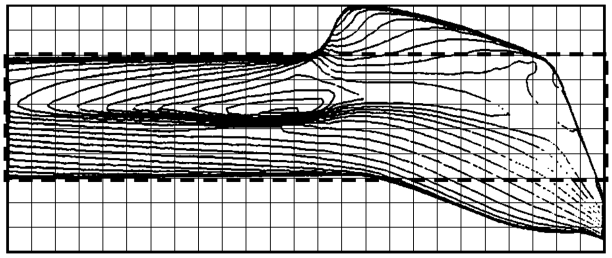

Fig. 9 Area comparison of the BERP blade.

a high rotational moment of inertia. By imposing the AI as an additional constraint, a more realistic blade shape can be obtained, because it has a tendency to have a sufficiently long chord length at the blade-tip region. In Eq. (4), the factors, except the moment of rotational inertia, are constant for a designed blade. Assuming uniform mass distribution along the span, the moment of rotational inertia is in proportion to the volume around the blade-tip region, so that the AI can be used to prevent a designed shape from having an excessively short chord length near the tip of the rotor blade. The AI value of the designed blade should be larger than 27, which is that of the baseline blade shape.

D. Design Variable Sampling

To produce a well-distributed set of initial DVs using a random number generator, the improved hypercube sampling routine [37] is used, where each set of DVs is generated using geometric relations and constraints. While generating the DVs, the order can affect the stiffness of the randomness in each DV; for example, if the generation of the leading-edge points randomly starts from point 1 (DV1), the next generation for point 2 would have a smaller range for the random generator. Extending this, the last point along the x direction, DV5, may have significantly less freedom in generating the random numbers. To avoid this number biasing effect, the order of the random number generation is defined as shown in Fig. 11, where the numbers on the upper part of Fig. 11 show the order of the control point definitions. Control point 1 and point 10 (DV1, DV14) do not affect the stiffness of the randomness in the other DVs, as they have independent regions. Point 3 (point 8 on the trailing edge) is located between its boundaries at first, and then point 2 (point 9) is defined between point 1 (point 10) and point 3 (point 8), and point 4 (point 7) is defined between point 3 (point 8) and point 5 (point 6). The random number generation for the edge of the rotor tip is repeated in reverse order, which accounts for two different patterns in generating the DVs, as shown in Fig. 11. This generator can produce various planform shapes, as summarized in Fig. 12.

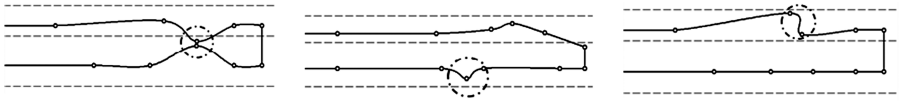

a) Minimum chord length limitation **b) Spline limitation** **c) Curvature limitation**

Fig. 10 Example of discarded blade shapes.

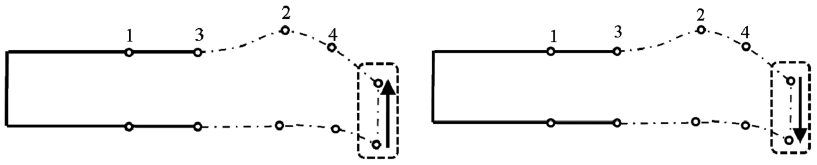

Fig. 11 Two order patterns in generating DVs.

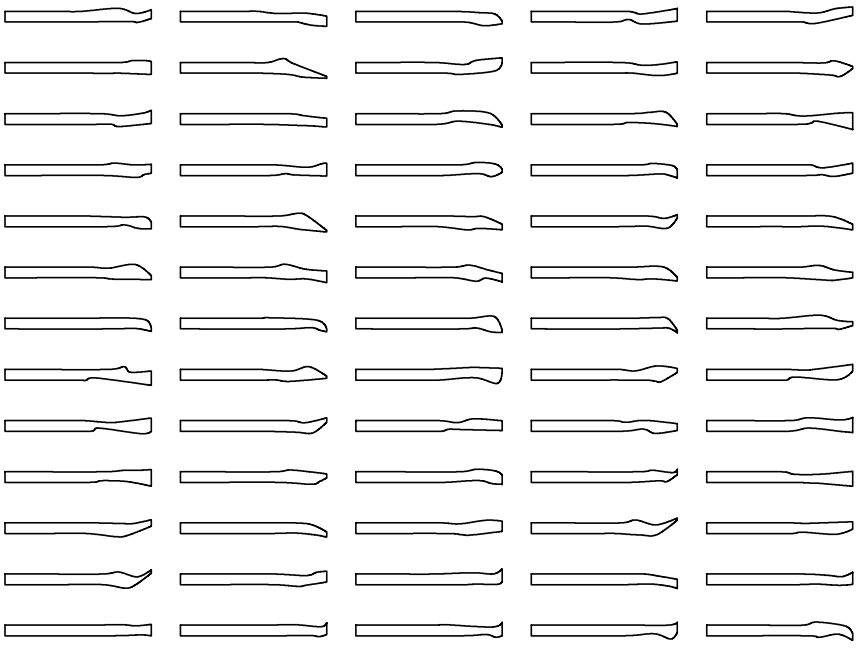

Fig. 12 Initial sampling planform.

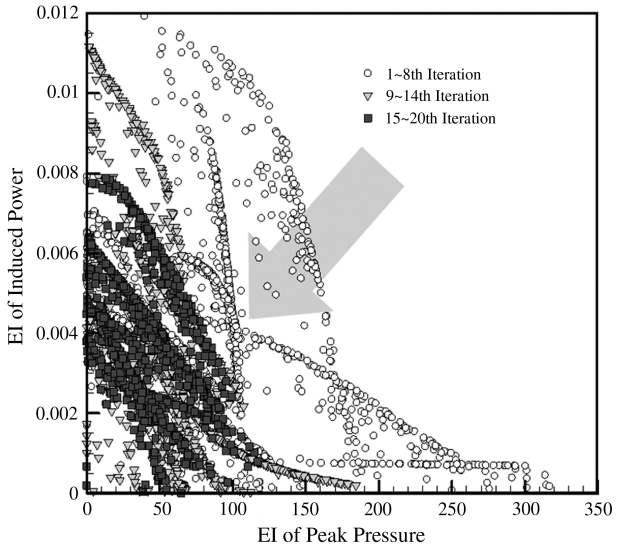

Fig. 13 Change of EI values on design process.

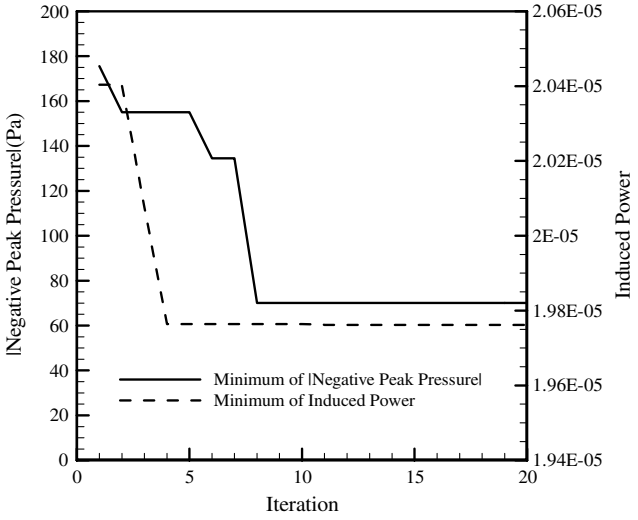

Fig. 14 Change of minimum objective values.

A total of 2000 blade planforms (i.e., 1000 sampling data for each pattern) are generated and checked to see if the constraints are met. Among them, only 65 blade planforms survive, as shown in Fig. 12, and these are used as the initial generation for the beginning of the optimization process. This figure shows that the present definition of the DVs can generate various planform shapes.

However, the present method has a problem in that some DVs do not have an effect independently on the blade shape. Conventional DVs are the taper ratio, the level of the swept back, the twist, etc., and each variable has a precise role in generating the blade shape, which is not affected by other variables; but the DVs in this work are affected by the position of the neighboring DVs, so it is considered that each DV does not have an independent effect, but there is significant cross coupling. This defect causes problems in analyzing the effects of the DVs on the objectives or the constraints, as discussed in Sec. V.

V. Design Results and Discussion

Throughout the optimization process, $2 \sim 4$ sample points are added to sequentially improve the kriging model every iteration using the EI. With the inclusion of the sample points, the accuracy of the kriging model is also enhanced while, at the same time, the EIs of sample points are decreased because of the uncertainty of the surrogate model, and the probability to become an optimum are reduced. Figure 13 shows the reduction of the EI values on the Pareto surface obtained over the iterations during the design process.

The theoretical convergence can be achieved when EI becomes less than 1% of the current best function value [35], but this is an extremely difficult criterion to achieve in practice, especially for this kind of multiobjective design. Thus, the convergence to the minimum of the objective at each iteration step is used as a practical criterion, and Fig. 14 shows the convergence of the minimum value of two objective functions, and it can be seen that the minimum values are converged for both objectives from about the 10th iteration.

After 20 iterations of the optimization procedure, 110 sample points are obtained, which indicates the number of CFD module calculations needed to be carried out; this evaluation number can be considered as quite significant in the amount of calculations needed for the optimization process. While an optimization procedure using only GAs will require 51,200 evaluations of the CFD module, because of the 100 generations with 512 populations, the efficiency of using the kriging-model-based GA method is confirmed to have 99.8% less calculation loads, which is a major improvement.

Before the design results are presented, the validity of using the kriging model is confirmed by cross validation [35]. Figures 15a and

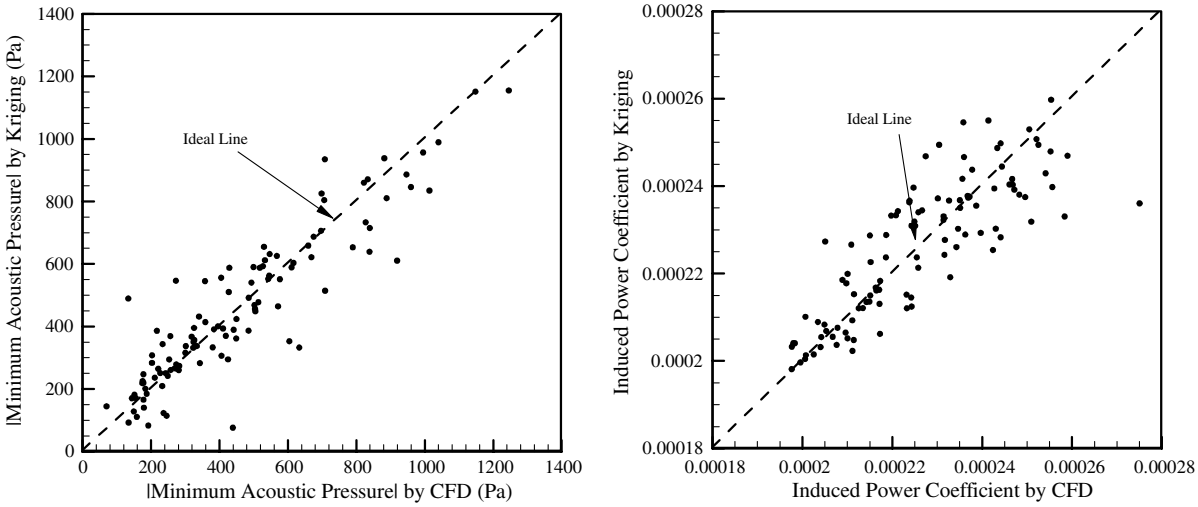

a) Minimum Acoustic Pressure **b) Induced Power Coefficient**

Fig. 15 Comparison between the CFD solver and the kriging model by cross validation.

15b illustrate the comparison of the objective values calculated by the CFD solver and those predicted by the kriging model. If all the points are located near the straight diagonal line of the x and y axis, the kriging model can be considered to be accurate. It can be seen that most of the sample points are located near the ideal lines, shown in Figs. 15a and 15b. Although the discrepancy seems to be greater in the range of higher induced power coefficients in Fig. 15b, these regions do not affect the searching process to determine the optimum, because the lower induced power region has a higher possibility of containing the optimum so the kriging models of the two objectives can be considered to be qualitatively accurate.

Standardized cross-validated residuals [35] provide quantitative evaluation of each objective function of the kriging model, as shown in Fig. 16, where the standardized cross-validated residuals are expressed as follows:

$$\frac{y(x_i) - \hat{y}_{-i}(x_i)}{s_{-i}(x_i)} \tag{5}$$

where x_i means the ith sample point, $y(x_i)$ is the value calculated by CFD solver, and $\hat{y}_{-i}(x_i)$ and $s_{-i}(x_i)$ are the estimated value and the root-mean-squared error of the kriging model without x_i, respectively.

In the kriging model, $s_{-i}(x_i)$ means standard deviation σ including uncertainty at the ith sample point, and about 99.7% of the confidence level is within $\pm 3\sigma$ in the normal distribution [35]. Most of the residual points for both objective functions using the kriging models lie in the interval $[-3, 3]$, which means that each kriging model has a confidence of 99.7%; even though only one point is located out of the confidence boundary in Fig. 16a, this point has no effect on the optimization, because it has a large value for the objective function.

The objective function values of the total sample points are shown in Fig. 17, which clearly summarizes the progression of the design optimization process. The values of the reference planform shapes, the baseline, the BERP type, the National Aerospace Laboratory (currently Japan Aerospace Exploration Agency; JAXA) (NAL) type, and the ONERA type are also presented for comparison. These planform shapes are similar to those of existing blades, but the airfoils of the reference blades are fixed as NACA0012. The planform shape in previous research [28] is also added, which is obtained based on the two objective functions to reduce HSI noise and to increase the blade loading and the airfoil thickness transition from NACA0012 at the root to NACA0008 at the tip.

It is clearly seen in Fig. 17 that additional sample points have better objective values than those of the initial samples and the reference shapes. Among these, three designed shapes are selected on the boundary of the minimum objective values, and Table 3 summarizes

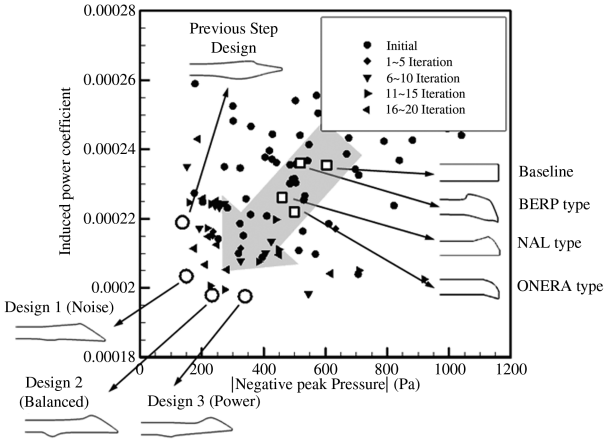

Fig. 17 The objective values of the sample points.

more specific objective values of the designed shapes. The designed shapes have similar levels of HSI noise reduction to those of the previous designed shapes, but the induced power coefficients of the present designed shapes are much less than those of the previous ones.

Interestingly, common features of the designed shapes are the sweptback angle and the high taper ratio near the tip, as shown in Fig. 18, which shows specific values of the sweptback angle and the taper ratio near the tip of the designed shapes. The average sweptback angle and taper ratio values of each designed shape are $\approx 23^\circ$ and ≈ 8.7, respectively. These shape features are the main design factors in reducing the HSI noise. Detailed explanations are given next, along with the acoustic pressure distributions and the Mach contours.

Figure 19 shows a comparison of the acoustic pressure distributions for each rotor blade, calculated by Kirchhoff's method where the change of the acoustic pressure on one blade shape is affected by the shock wave, which is propagated from the blade tip. For higher sweptback angles of each blade, this occurs at a later time on the x axis for the minimum peak, as shown in Fig. 19. The stronger shock waves generate more abrupt changes of acoustic pressure and give lower minimum peak pressures. The absolute values of the minimum acoustic pressure for the optimum shapes are reduced by more than 50% compared with the baseline. These results show that the HSI noise of each optimum shape is reduced considerably compared with that of the baseline.

The Mach contours of the baseline and the three designed shapes are also compared in Fig. 20, where it can be seen that the size of the supersonic region in the vicinity of the blade tip is proportional to the strength of the shock wave. The supersonic region of the designed

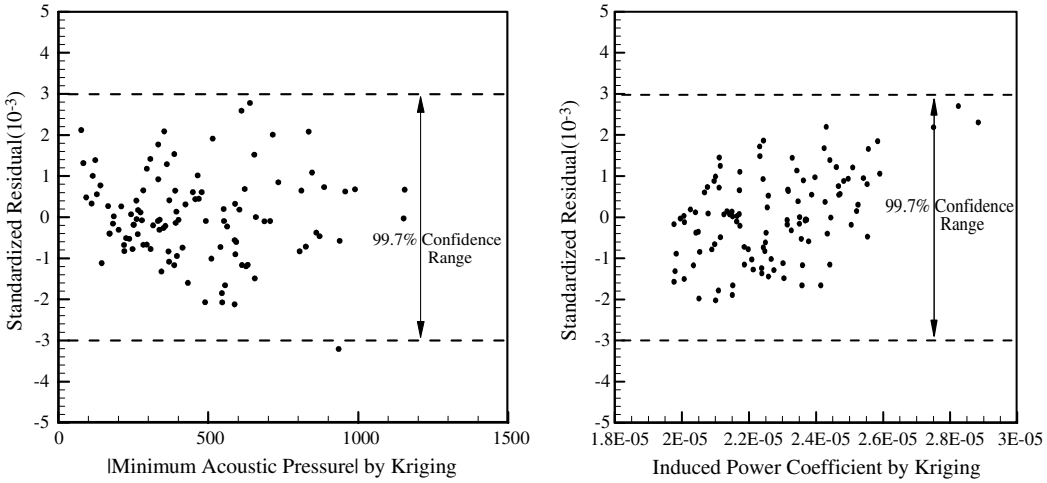

a) Minimum Acoustic Pressure **b) Induced Power Coefficient**

Fig. 16 Standardized cross-validated residuals.

Table 3 Objective function values for each blade shape[a]

Shape	Peak pressure, Pa	C_{Pi}
Baseline	750(0%)	0.0002355(0%)
Previously designed [19]	161(−79%)	0.0002190(−7%)
Design 1 (noise)	150(−80%)	0.0002034(−13.6%)
Design 2 (balanced)	233(−69%)	0.0001980(−15.9%)
Design 3 (power)	340(−55%)	0.0001976(−16.1%)

[a]The percentage in parentheses represents the difference from the value of the baseline.

shapes is smaller than that of the baseline, and the chordwise size of the supersonic region is dependent on the taper ratio, which decreases the intensity of the HSI noise. The chordwise width of the supersonic region in Fig. 20d is larger than that of the other designed shapes, because design 3 (power) has a small taper ratio. The location of the supersonic region is moved to the blade tip due to the sweptback angle. Figure 20b shows the supersonic region of design 1 is almost inclined toward the tip of the blade, which has the highest sweptback angle among the designed shapes and the extent of the delocalization is increased from Figs. 20b–20d, which have the smallest sweptback angles and taper ratios. Therefore, it is concluded that two design features, namely, the sweptback angle and the taper ratio, are effective in reducing the strength of the HSI noise.

The ideal induced power is obtained if the load distribution is uniform along the span so that the relative comparison of the induced powers can be seen from the circulation distribution along the radial direction. Figure 21 compares the normalized circulation distribution of each blade, and the baseline has a peak of circulation near the tip and the largest induced power coefficient. On the other hand, from design 1 to design 3, the peak circulations are substantially reduced, and the circulation distribution becomes almost a plateau in the

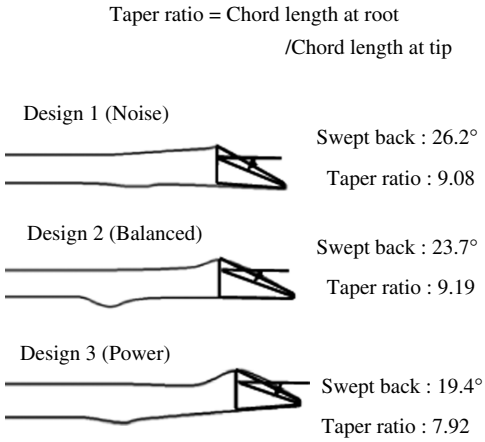

Fig. 18 Sweptback angle and taper ratio of designed shapes.

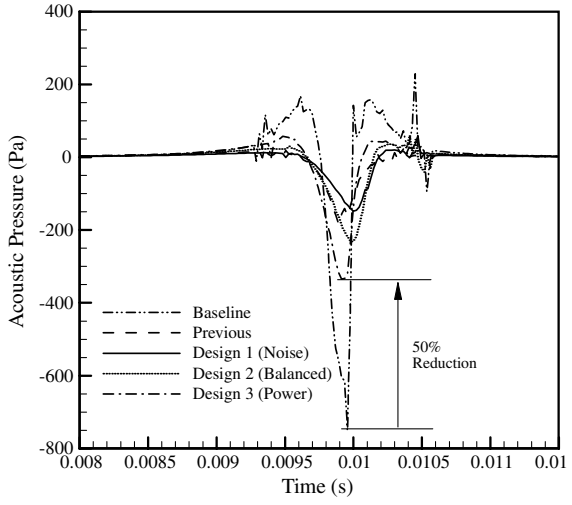

Fig. 19 Acoustic pressure for each designed blade shape.

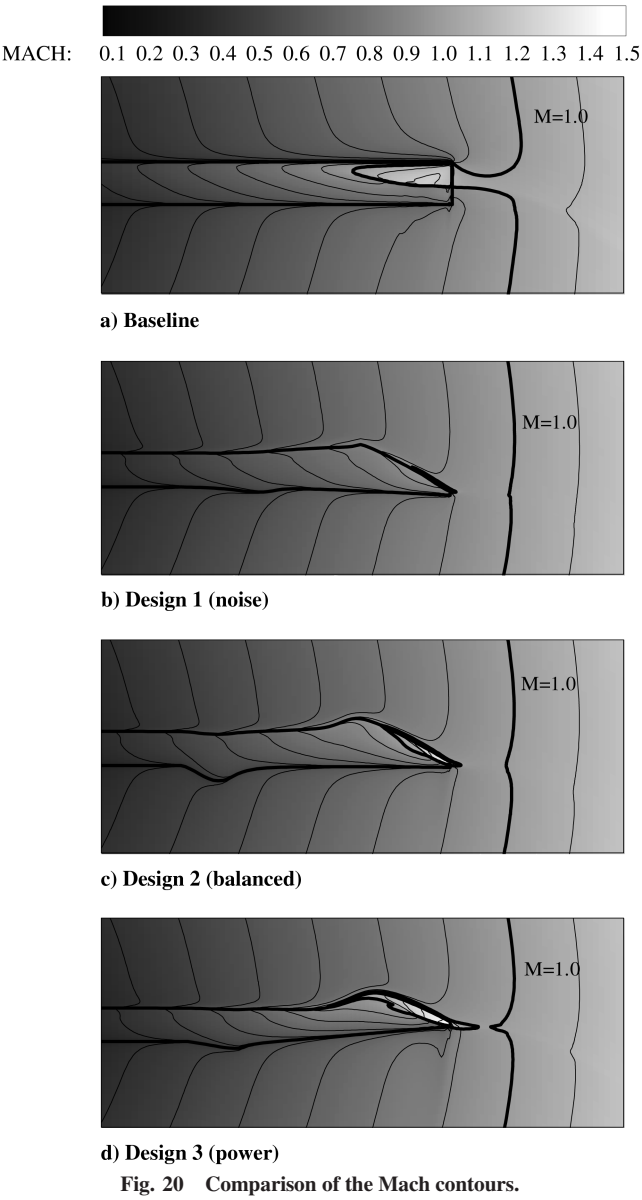

Fig. 20 Comparison of the Mach contours.

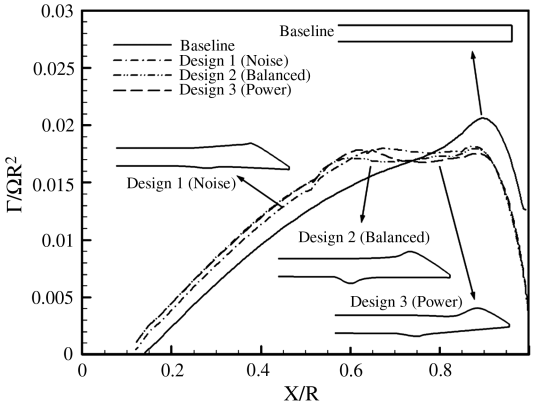

Fig. 21 Comparison of the circulation distribution.

Table 4 Airfoil section and transition point[a]

	Camber		Thickness		
Shape	Root	Tip	Root	Tip	Transition position
Design 1 (noise)	0.0234	0.0171	0.1496	0.0805	0.7067
Design 2 (balanced)	0.0196	0.008	0.1488	0.1154	0.5722
Design 3 (power)	0.0181	0.0101	0.1485	0.1495	0.6689

[a]All values of the airfoil are nondimensionalized by the chord length, while the transition position is nondimensionalized by the radius length.

Table 5 Planform areas and AIs of each blade shape designed[a]

Shape	Area	AI
Baseline	0.079652(0%)	27.312
Design 1 (noise)	0.080798(+1.4%)	28.184
Design 2 (balanced)	0.082319(+3.3%)	33.947
Design 3 (power)	0.077719(−2.4%)	33.162

[a] All values are nondimensionalized by the radius length. The percentage in parentheses represents the difference from the value of the baseline.

region from 0.6*R* to 0.9*R*, which seems to be achieved by the wedgelike shape on the blade tip. The relatively uniform distribution of the circulation at the outboard region has the effect of reducing the induced power of the rotor, and Table 3 shows that the designed rotor blades have almost 15% lower induced power than the baseline blade.

In the present work, the camber and the thickness of the airfoils on the tip and the root are considered as additional DVs, and Table 4 shows the specific values of the airfoils and the transition positions. The thickness of the root airfoil in each designed shape has a high value for satisfying the AI constraint and for reducing the induced power. The root airfoil of the designed shapes has a larger camber than that of the tip airfoil, and the thickness and chamber of the root airfoil lead to an increased circulation distribution below 0.6*R*, as shown in Fig. 21, whereas for the same thrust level, increased circulation below 0.6*R* can reduce the peak circulation value. Thus, it is possible to reduce the induced power of the rotor blade. As expected, the tip airfoils have lower camber than the root airfoils, because the camber tends to strengthen the intensity of shock waves at the tip region. For the same reason, the thickness on the tip airfoil is also decreased, except in design 3, where to satisfy the AI constraint, it has a thicker airfoil on the tip airfoil because of its relatively small area, as shown in Table 5.

It is evident from the results that the change of the airfoil shape and the transition of the two airfoils help to achieve improved objectives and to satisfy the constraint, simultaneously.

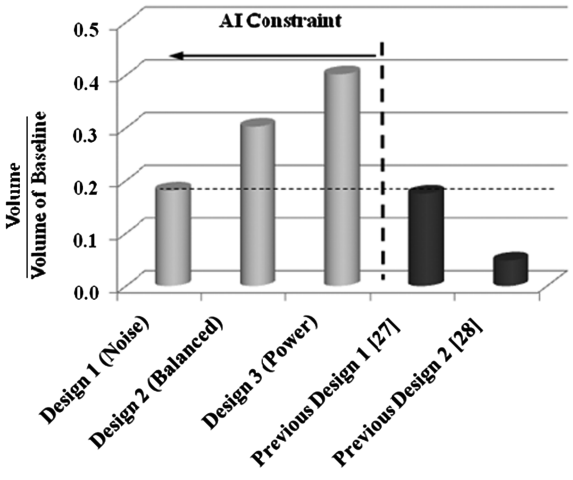

Fig. 22 Comparison of the volumes near the blade tip.

As mentioned earlier, the AI constraint is imposed in the present optimization process and, to retain some designated AI value, the rotor blade should have sufficient volume at the tip region. Comparisons are made in Fig. 22 to determine the relative tip region volume of five blade configurations, of which three are from the present optimization and two are from previous studies. The tip region volume is obtained from 0.925*R*, because this is the starting location of decreasing the chord length on the previous design 1 [27], as shown in Fig. 23a. The values on the *y* axis are nondimensionalized values by the volume of the baseline, and the optimized configurations in the present study have larger volumes than the previous configurations because of the AI constraint.

Figure 23a comparatively shows the overall planform shape of two presently designed shapes and two previously designed shapes. From the short chord length near the tip, the previously designed shapes have a smaller AI than those of the shapes designed here. The specific values and tip shapes are shown in Fig. 23b, where the chord

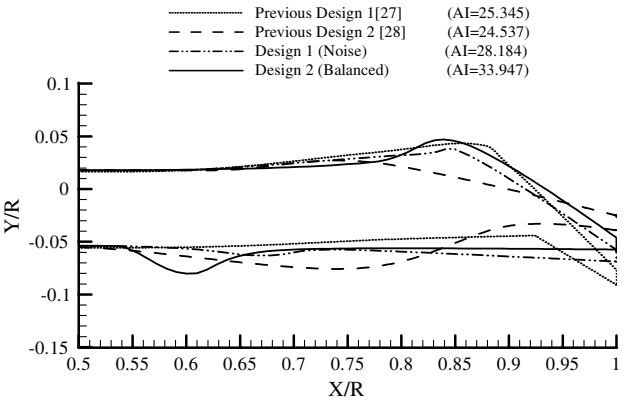

a) Overall planforms

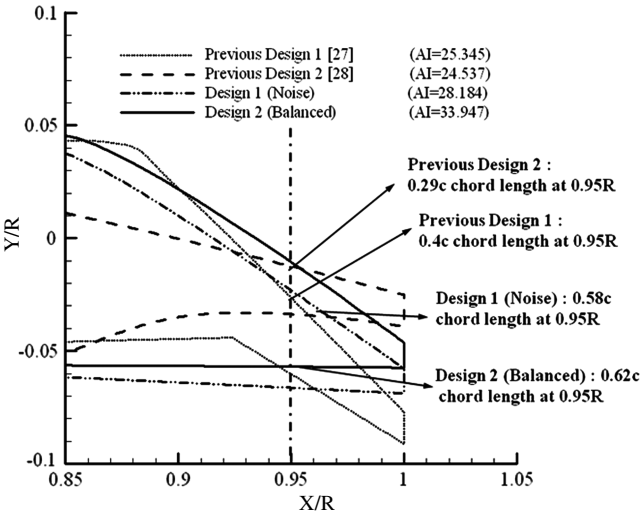

b) Magnified shapes near the tip

Fig. 23 Comparison of the planform shapes.

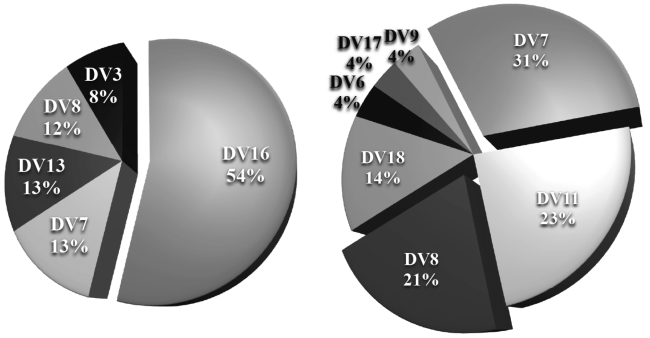

a) HSI Noise b) Induced Power

Fig. 24 ANOVA results.

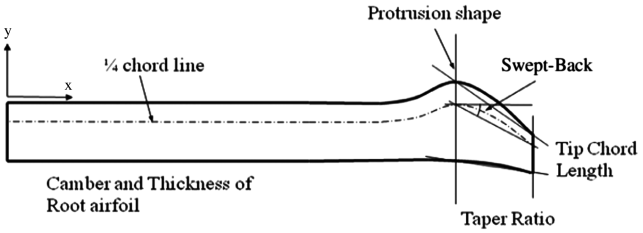

Fig. 25 Design shape features for SOM.

lengths at $0.95R$ of the presently designed blades are 1.5 times longer than those of the previously designed shapes. This means that the AI constraint plays an effective role in preventing the blade-tip chord length from becoming excessively short.

To identify the effect of each DV on the objectives, the analysis of variance (ANOVA) has been performed, as in Fig. 24. Once the kriging models are obtained, the effects of each DV on the objective function can be calculated by decomposing the total variance of the model into the variance components due to that DV. The DVs and their interactions with the proportions to the total variance are over 2%, as shown in Fig. 24. According to the ANOVA results, DV 7, DV 8, and DV 11 are the most important DVs in reducing HSI noise. As shown in Fig. 9, DV 7 and DV 8 control the tip chord length, which is directly connected to reducing the strength of the shock wave at the tip, but it is not easy to identify the effects of DV 11 clearly, because the DV depends on the relative values of the neighboring DVs. For the induced power, the thickness of the root airfoil (DV 16) is found to be the most important DV. As mentioned previously, a thick airfoil gives increased circulation distribution around $0.6R$ to substantially reduce the induced power.

To avoid the dependency problem of the DVs, the design shape features are redefined, as shown in Fig. 25, where this redefinition follows conventional rotor design factors, such as the sweptback angle, the taper ratio, the tip chord length, etc. This redefinition can clarify the influence analysis to objectives or constraints of a single design feature, because the design features do not affect the other features, but they do not include the kriging model or have static values for the ANOVA. Thus, a self-organization map (SOM) is introduced for analyzing the design features. The SOM is an unsupervised neural network technique to classify, organize, and visualize large data sets; it is a nonlinear projection algorithm [38] from high- to low-dimensional spaces where the projection is based on self-organization of a low-dimensional array of the neurons. In the projection algorithm, the weights between the input vector and the array of the neurons are adjusted to represent features of the high-dimensional data on low-dimensional maps. The closer the two patterns are in the original space, the closer the response of the two neighboring neurons in the low-dimensional space, so that the SOM reduces the dimensions of the input data while preserving their features. The reorganized data can suggest colored maps by which the relations or the influences among input data are analyzed.

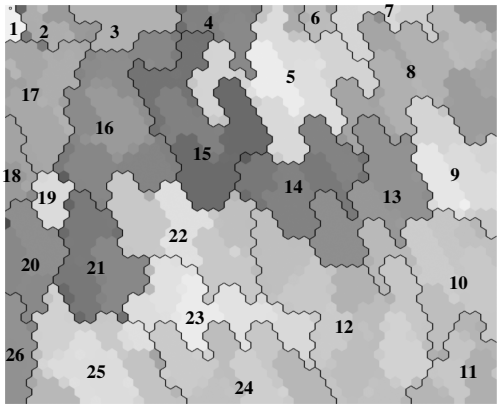

Fig. 26 SOM classified by 25 clusters.

Figure 26 shows the SOM classified into 26 clusters based on the similarity with regard to two objective functions and one constraint. The x and y coordinates of the SOM have no meaning, and the clusters are arranged arbitrarily to be included in a rectangular frame. From this figure itself, it is impossible to extract any information about the design space; to obtain such information, the SOM is colored by the value of each objective function, as shown in Fig. 27. The SOMs colored by HSI noise, induced power, and AI show smooth and continuous distributions, because they are arranged by the similarity of two objectives and constraints, as shown in Figs. 27a–27c. Figure 27c shows the increasing tendency of the AI, from right to left and the clusters on the right of the SOM: 5 (a half of), 6, 8, 9, 10, 11 (except a small part), 13, 14, and 19 do not satisfy the AI constraint. The shadow region indicates this infeasible design space in Fig. 27. The low values of the HSI noise are distributed on clusters 11, 12, 24, 25, and 26, and the low values of the induced power are distributed on clusters 11, 21, 22, and 24. Among these clusters, design 1 is located on cluster 11, and the other designed shapes are located on cluster 24. These two clusters are compromised regions between the two objectives.

Comparison among the objectives and design shape features suggests that the taper ratio, the sweptback angle, the protrusion shape, the tip chord length, and the thickness and camber of the root airfoil are the important features in improving the acoustic and aerodynamic performances simultaneously. The SOM colored by the taper ratio, shown in Fig. 27d, has the reverse distribution of the SOM colored by the tip chord length, shown in Fig. 27g, implying that the tip chord length is dominant with respect to the taper ratio. These shape features affect the HSI noise, because the high (taper ratio) or the low (tip chord length) values are distributed on clusters 24 and 25.

The sweptback angle is converted as $|\text{sweptback angle} - 10^\circ|$ onto the SOM, so that clusters 12, 19, 20, 21, 23, 24, 25, and 26 represent near 10° in Fig. 27e. Although the clusters of the low sweptback angle (converted) do not have the low value of the HSI noise, the clusters (19, 21, 23, 24) of the low HSI noise have the low converted sweptback angles in Fig. 27e. These results with the shape features of designed blade in Figs. 18 and 20 show that the planform of low HSI noise has sweptback angles from 10 to 25°.

The protrusion shape means the degree of the protruded leading edge is near the tip, and Fig. 27f shows strong protrusion shapes on clusters 11, 21, 22, 23, and 24. We showed the effects of the protrusion of the leading edge on the induced power in Fig. 21, and the distributions of the strong protrusion shape in Fig. 27f are similar to those of the SOM colored by the induced power. Therefore, it can be confirmed that the protrusion shape helps to reduce the induced power of the blade, as mentioned previously.

Figures 27h and 27i indicate that the camber and thickness of the root airfoil also have similar distributions of induced power. These design features also reduce the induced power and increase the lift from the root to $0.6R$ of the rotor, as mentioned previously. These results agree with those from the ANOVA.

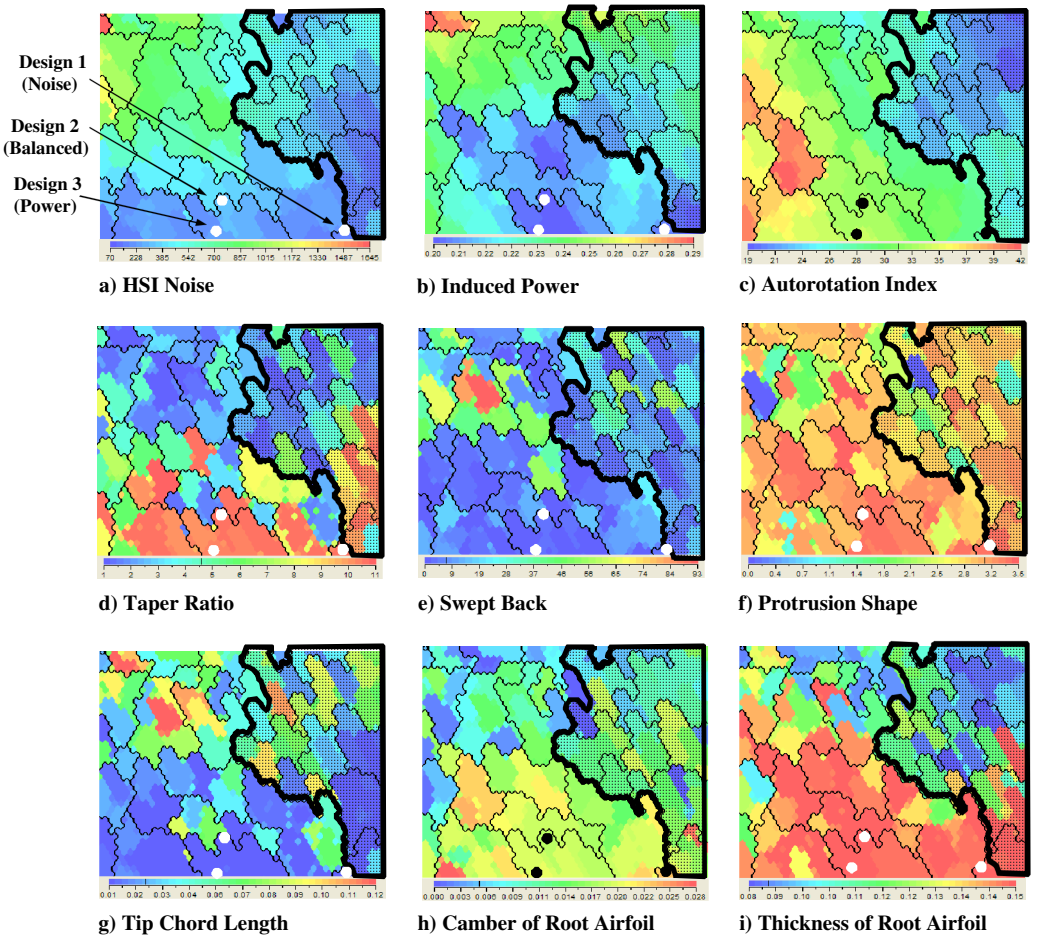

Fig. 27 SOM results.

VI. Conclusions

The paper has presented a study to obtain improved helicopter blade shapes via numerical optimization, which can simultaneously reduce the HSI noise and the induced power. To obtain more general and practical rotor blade configurations, a novel constraint for AI and additional DVs to describe the airfoil changes along the span have been introduced. By performing a thorough analysis of the design process and the results presented, the following conclusions are reached:

1) Using GAs with the kriging model gives a more efficient design (99.8% reduction in the calculation loads), and more robust designs can be achieved than by using only GAs. From the optimized results, three design shapes have been obtained that lie on the boundary of the minimum performances for both objectives. One of these final designs for the rotor blade configurations shows dramatic reductions in the HSI noise by 82% (−14 dB; baseline = 152 dB, design for noise = 138 dB) without any severe sacrifices of aerodynamic performance. Another blade planform design shows considerable reduction of induced power of 16.1%. These shapes are located on the tradeoff relation between the generation of HSI noise and induced power. All three blade shape designs show improved performances over the reference and baseline shapes, and the common features of the designed shapes for these improvements are found to be ≈23° sweptback angle and ≈8.7 taper ratio.

2) For the acquisition of a practical blade shape, the AI constraint and the DVs for two airfoils section changes are added. In previous research, the designed shapes had the defect of the chord length around the blade tip becoming so short that it could lead to structural problems; introducing the AI constraint was imposed in the present work to avoid this, and the resulting designed shapes have a larger volume and longer chord lengths on the tip region than those of previously designed shapes. The airfoils have different thickness and camber on the root and the tip, thereby helping to archive improved performances as well as to satisfy the constraints. The camber and thickness of the root airfoil help in generating uniform circulation distributions at $r/R > 0.6$ for minimizing the induced power, so that the additional design constraint and variables are useful to design more practical blades.

3) By using ANOVA and SOM approaches, the effect of each DV or each shape feature to achieve the design objectives is analyzed. By performing an ANOVA, it is deduced that the tip chord length and the thickness of the root airfoil are important DVs for HSI noise and induced power reduction, respectively, but the effects of the other DVs for arbitrary planforms are not clear. This is because the effect of each DV is dependent on that of the others. By applying the design shape features on the SOM, the important features that effect the design objectives can be extracted to show that the taper ratio, the sweptback angle, and the tip chord length have the major effect to reduce the HSI noise, and the protrusion shape, the camber, and the thickness of the root airfoil have the strongest effect on the decreasing the induced power. These results agree with those from the ANOVA analysis in the first and second conclusions.

The present study can be extended to the multidisciplinary blade design optimization for general flight applications such as for forward flight or the blade–vortex interaction flight condition.

Acknowledgments

This study was supported under the Brain Korea 21 Project and the Korea Aerospace Research Institute under the Korean Helicopter Program Dual-Use Component Development Program funded by the Ministry of Knowledge Economy.

References

[1] Leishman, J. G., *Principle of Helicopter Aero-Dynamics*, Cambridge Univ. Press, New York, 2000, Chaps. 1, 6.

[2] George, A. R., "Helicopter Noise: State of the Art," AIAA Paper 1977-1337, 1977.

[3] White, R. P., "The Status of Rotor Noise Technology," *Journal of the American Helicopter Society*, Vol. 25, No. 1, 1980, pp. 22–29. doi:10.4050/JAHS.25.22

[4] Schmitz, F. H., and Yu, Y. H., "Helicopter Impulsive Noise: Theoretical and Experimental Status," NASA TM 84390; also U. S. Army TR USAAVRADCOM TR 83-A-2, Nov. 1983.

[5] Ffowcs Williams, J. E., and Hawkings, D. L., "Sound Generation by Turbulence and Surface in Arbitrary Motion," *Philosophical Transactions of the Royal Society of London, Series A: Mathematical and Physical Sciences*, Vol. 264, No. 1151, 1969, pp. 321–342. doi:10.1098/rsta.1969.0031

[6] Farassat, F., "Theory of Noise Generation from Moving Bodies with an Application to Helicopter Rotors," NASA TRR-451, 1975.

[7] Nakamura, Y., and Azuma, A., "Rotational Noise of Helicopter Rotors," *Vertica*, Vol. 3, Nos. 3–4, 1979, pp. 293–316.

[8] Boxwell, D. A., Yu, Y. H., and Schmitz, F. H., "Hovering Impulsive Noise: Some Measured and Calculated Results," *Vertica*, Vol. 3, No. 1, 1979, pp. 35–45.

[9] Hanson, D. B., and Fink, M. R., "The Importance of Quadrupole Sources in Prediction of Transonic Tip Speed Propeller Noise," *Journal of Sound and Vibration*, Vol. 62, No. 1, 1979, pp. 19–38. doi:10.1016/0022-460X(79)90554-6

[10] Schmitz, F. H., and Yu, Y. H., "Transonic Rotor Noise: Theoretical and Experimental Comparison," *Vertica*, Vol. 5, No. 1, 1981, pp. 55–74.

[11] Aggarwal, H. R., "The Calculation of Transonic Rotor Noise," *AIAA Journal*, Vol. 22, No. 7, 1984, pp. 996–998. doi:10.2514/3.8722

[12] Prieur, J., "Calculation of Transonic Rotor Noise Using Frequency Domain Formulation," *AIAA Journal*, Vol. 26, No. 2, 1988, pp. 156–162. doi:10.2514/3.9867

[13] George, A. R., and Lyrintzis, A. S., "Mid-Field and Far-Field Calculations of Transonic Blade–Vortex Interactions," AIAA 10th Aeroacoustics Conference, AIAA Paper 86-1854, July 1986.

[14] George, A. R., and Lyrintzis, A. S., "Acoustics of Transonic Blade–Vortex Interactions," *AIAA Journal*, Vol. 26, No. 7, 1988, pp. 769–776. doi:10.2514/3.9968

[15] Xue, Y., and Lyrintzis, A. S., "Rotating Kirchhoff Formulation for Three-Dimensional Transonic Blade Vortex Interaction Hover Noise," *AIAA Journal*, Vol. 32, No. 7, 1994, pp. 1350–1359. doi:10.2514/3.12202

[16] Lyrintzis, A. S., "Review: The Use of Kirchhoff's Method in Computational Aeroacoustics," *Journal of Fluids Engineering*, Vol. 116, No. 4, 1994, pp. 665–676. doi:10.1115/1.2911834

[17] Philippe, J. J., and Vuillet, A., "Aerodynamic Design of Advanced Rotors with New Tip Shapes," *39th Annual Forum of the American Helicopter Society*, AHS International, Alexandria, VA, May 1983, pp. 267–277.

[18] Polacsek, C., Zibi, J., and Costes, M., "Helicopter Rotor Noise Predictions Using 3D Computed Aerodynamic Data for Different Blade Geometries," *Proceedings of the 19th European Rotorcraft Forum*, Paper B3-1–B3-11, Como, Italy, Sept. 1993.

[19] Baeder, J. D., Gallman, J. M., and Yu, Y. H., "A Computational Study of the Aeroacoustics of Rotors in Hover," *Journal of the American Helicopter Society*, Vol. 42, No. 1, 1997, pp. 39–53. doi:10.4050/JAHS.42.39

[20] Aoyama, T., Aoki, M., Kondo, N., Saito, S., and Kawachi, K., "Effect of Blade-Tip Shape on High-Speed Rotor Noise," AIAA Paper 1996-2380, 1996.

[21] Purcell, T. W., "CFD and Transonic Helicopter Sound," *Proceedings of the 14th European Rotorcraft Forum*, Milan, Italy, Sept. 1988, pp. 2-1–2-17.

[22] Jones, B. R., Crossley, W. A., and Lyrintzis, A. S., "Aerodynamic and Aeroacoustic Optimization of Airfoils via a Parallel Genetic Algorithm," *Journal of Aircraft*, Vol. 37, No. 6, 2000, pp. 1088–1096. doi:10.2514/2.2717

[23] Lee, S. W., and Kwon, O. J., "Aerodynamic Shape Optimization of Hovering Rotor Blades in Transonic Flow Using Unstructured Meshes," *AIAA Journal*, Vol. 44, No. 8, Jan. 2006, pp. 1816–1825. doi:10.2514/1.15385

[24] Le Pape, A., "Numerical Aerodynamic Optimization of Helicopter Rotors: Multi-Objective Optimization in Hover and Forward Flight Conditions," *31st European Rotorcraft Forum*, Florence, Italy, Sept. 2005, pp. 98.1–98.3.

[25] Xue, S., Docker, B., and Narramore, J., "Integrated Aero-Acoustics Rotor Simulation and Design Optimization," 12th AIAA/CEAS Aeroacoustics Conference (27th AIAA Aeroacoustics Conference), AIAA Paper 2006-2603, May 2006.

[26] Collins, K., Bain, J., Sankar, L., Egolf, T. A., Janakiram, R. D., Brentner, K., and Lopes, L., "Pareto Frontier Method for Multi-Disciplinary Optimization of Helicopter Rotors," *American Helicopter Society Specialist's Conference on Aeromechanics*, AHS International, Alexandria, VA, Jan. 2008.

[27] Yang, C., Aoyama, T., Chae, S., Yee, K., Jung, S., and Obayashi, S., "Blade Planform Optimization to Reduce HSI Noise of Helicopter in Hover," *64th Annual Forum of the American Helicopter Society*, AHS International, Alexandria, VA, April 2008.

[28] Chae, S., Yee, K., Yang, C., Aoyama, T., Jung, S., and Obayashi, S., "Blade Shape Optimization for HSI Noise Reduction and Performance Improvement of Helicopter," *34th European Rotorcraft Forum* [CD-ROM], Royal Aeronautical Society, Hampshire, U.K., Sept. 2008.

[29] Aoyama, T., Kawachi, K., and Saito, S., "Unsteady Calculation for Flow-Field of Helicopter Rotor with Various Tip Shapes," *18th European Rotorcraft Forum*, ONERA Paper B03, Paris, Sept. 1992.

[30] Farassat, F., "Generalized Functions and Kirchhoff Formulas," 2nd AIAA/CEAS Aeroacoustics Conference (17th AIAA Aeroacoustics Conference), AIAA Paper 1996-1705, 1996.

[31] Farassat, F., "Acoustic Radiation from Rotating Blade: The Kirchhoff Method in Aeroacoutics," *Journal of Sound and Vibration*, Vol. 239, No. 4, 2001, pp. 785–800. doi:10.1006/jsvi.2000.3221

[32] Jeong, S., Murayama, M., and Yamamoto, K., "Efficient Optimization Design Method Using Kriging Model," *Journal of Aircraft*, Vol. 42, No. 2, 2005, pp. 413–420. doi:10.2514/1.6386

[33] Jeong, S., and Obayashi, S., "Multi-Objective Optimization Using Kriging Model and Data Mining," *KSAS International Journal*, Vol. 7, No. 1, May 2006, pp. 1–12.

[34] Jeong, S., Obayashi, S., and Yamamoto, K., "Aerodynamic Optimization Design with Kriging Model," *Transactions of the Japan Society for Aeronautical and Space Sciences*, Vol. 48, No. 161, Nov. 2005, pp. 161–168. doi:10.2322/tjsass.48.161

[35] Donald, R. J., Matthias, S., and William, J. W., "Efficient Global Optimization of Expensive Black-Box Function," *Journal of Global Optimization*, Vol. 13, No. 4, 1998, pp. 455–492. doi:10.1023/A:1008306431147

[36] Goldberg, D. E., *Genetic Algorithms in Search, Optimization and Machine Learning*, Addison Wesley Longman, Reading, MA, 1989.

[37] Beachkofski, B. K., and Grandhi, R. V., "Improved Distributed Hypercube Sampling," 43rd AIAA/ASME/ASCE/AHS/ASC Structures, Structural Dynamics, and Materials Conference, AIAA Paper 2002-1274, April 2002.

[38] Krzysztof, J. C., Witold, P., and Roman, W. S., *Data Mining Methods for Knowledge Discovery*, Kluwer Academic, Norwell, MA, 1998.